Quasi-1D Mn_2O_3 Nanostructures Functionalized with First-Row Transition Metal Oxides as Oxygen Evolution Catalysts

Lorenzo Bigiani,[†] *Chiara Maccato,*[*,†] *Teresa Andreu,*[§,∥] *Alberto Gasparotto,*[†] *Cinzia Sada,*[#] *Evgeny Modin,*[⊥] *Oleg I. Lebedev,*[▽] *Joan Ramon Morante,*[§,∥] *and Davide Barreca*[‡]

[†] Department of Chemical Sciences, Padova University and INSTM, 35131 Padova, Italy

[§] IREC, Catalonia Institute for Energy Research, 08930 Sant Adrià de Besòs, Barcelona, Catalonia, Spain

[∥] Universitat de Barcelona (UB), 08028 Barcelona, Spain

[#] Department of Physics and Astronomy, Padova University and INSTM, 35131 Padova, Italy

[⊥] CIC nanoGUNE BRTA, 20018 Donostia - San Sebastian, Spain

[▽] Laboratoire CRISMAT, ENSICAEN UMR6508, 14050 Caen Cedex 4, France

[‡] CNR-ICMATE and INSTM, Department of Chemical Sciences, Padova University, 35131 Padova, Italy

ABSTRACT: The development of cheap and efficient catalysts for the oxygen evolution reaction (OER) plays a critical role for sustainable energy conversion and storage. Herein, we report on Mn_2O_3-based systems supported on nickel foams and functionalized with first-row transition metal (Fe, Co, Ni) oxide nanoparticles (NPs) as OER electrocatalysts in alkaline media, fabricated by a plasma-assisted process. The remarkable substrate porosity and high Mn_2O_3 active area, due to the quasi-1D nano-organization, enabled an efficient ultra-dispersion of Fe_2O_3, Co_3O_4 and NiO NPs into Mn_2O_3 and an intimate oxide-oxide interfacial contact, enhancing thus charge carrier transport, and facilitating reactants and products diffusion. Among the developed systems, Fe_2O_3-Mn_2O_3 yielded the highest electrocatalytic activity, corresponding to a low overpotential of ≈350 mV at 10 $mA \times cm^{-2}$ and a Tafel slope of ≈70 $mV \times dec^{-1}$, allowing high current density values. The obtained performances, discussed in relation to material properties, are superior to almost all state-of-the-art manganese oxide catalysts and compare favorably with various noble metal-based systems, paving the way to additional activity improvements *via* compositional and interfacial engineering.

KEYWORDS: Mn_2O_3, Fe_2O_3, Co_3O_4, NiO, plasma-assisted fabrication, oxygen evolution reaction

■ INTRODUCTION

The rapid and continuous increase of the global energy demand, along with the rising concern on environmental issues,[1-4] has drawn a considerable attention on alternative energy technologies, in order to minimize the dependency on unsustainable fossil fuels.[5-8] In this context, water electrolysis is one of the most efficient and environmentally friendly methods for the large-scale production of molecular hydrogen, considered as the clean energy carrier of the future.[4,9-11] Nevertheless, the current process bottleneck is the oxygen evolution reaction (OER), characterized by a high energy barrier and sluggish kinetics.[1,3,8,12-18] To date, the benchmark OER catalysts showing an excellent activity in alkaline environments are Ir- and Ru-based materials, but their high cost, low abundance and poor long-term stability[5,7,10,19-22] have stimulated the search for efficient alternatives based on earth-abundant elements.[2,23-25] To this regard, amenable candidates are first-row transition metal oxides, thanks to their unique 3*d* electronic structures and the possibility of yielding a stable O_2 evolution at modest overpotentials.[2,10,12,14,26] Among them, manganese oxides offer a rich variety of crystal structures and Mn oxidation states, whose tailoring is an important, though challenging, issue to develop effective electrocatalysts operating under basic conditions.[4,17,23,27-30] In particular, Mn_2O_3 is considered the most active manganese oxide thanks to the presence of highly distorted [MnO_6] octahedra, leading to a variety of Mn-O bond distances and an enhanced reactivity of Mn(III) d^4 centers in OER-related processes.[8,13-14,24,31] Indeed, Mn(III)-containing nanostructures with tailored defectivity feature labile Mn−O bonds, allowing an easier formation of OER intermediates and promoting the cleavage of Mn−O_2 adducts, which facilitates water oxidation reactions and increases the overall turnover frequency of the catalytic centers.[14,31]

So far, Mn_2O_3 OER electrocatalysts have been prepared both from powders eventually mixed

with binders/conductive species,[20,23,27-29,31-33] and as nanostructures/thin films directly grown onto suitable substrates.[6,11-15,21,24] Indeed, the latter systems represent a more practical choice, since they enable to prevent undesired aggregation/phase segregation phenomena and to overcome issues related to poor conductivity and durability, avoiding the use of binders that typically decrease conductivity.[3,6,19,24] To this aim, a suitable nanoscale engineering of the system architecture through versatile synthetic routes[16,29-30] can facilitate electron/mass transfer and ensure a high density of surface active sites, improving OER activity.[5-7,27] As water oxidation involves four different steps, each one with its energy barrier, the use of complementary catalysts can trigger the overall process, exerting a favorable promotional effect. Therefore, an additional synergistic mean to boost functional performances relies on the fabrication of multi-component Mn-based oxides, which outperform their single-phase counterparts thanks to the tuning of metal site redox properties and interfacial electron transfer phenomena at oxide-oxide interfaces.[2,11,19,26] In this regard, Mn_2O_3-based composites with Cr_2O_3,[8] MnO_2,[4] and RuO_2,[11,34] have been so far tested for OER electrocatalysis. Among the possible complementary catalysts, Fe, Co, and Ni oxides are well-known and attractive activators,[1,8,12,16,19-20,30,33,35] but, to our knowledge, no literature works on Mn_2O_3 OER electrocatalysts functionalized with Fe_2O_3 and NiO are available, whereas Co_3O_4-Mn_2O_3 anodes obtained from powder mixtures have been reported only once.[20]

In this work, Mn_2O_3 nanostructures decorated with Fe, Co and Ni oxides were fabricated on low-cost and high area nickel foam (NF) substrates, favorably acting as current collectors and favoring electrolyte diffusion and gas evolution during OER, thanks to their inherent porosity.[5,10] The adopted plasma-assisted synthesis procedure is illustrated in Figure 1a, and the pertaining details are reported in the Supporting Information. In particular, after the initial plasma enhanced-chemical vapor deposition (PE-CVD) of manganese oxide, Fe_2O_3, Co_3O_4, and NiO nanoparticles

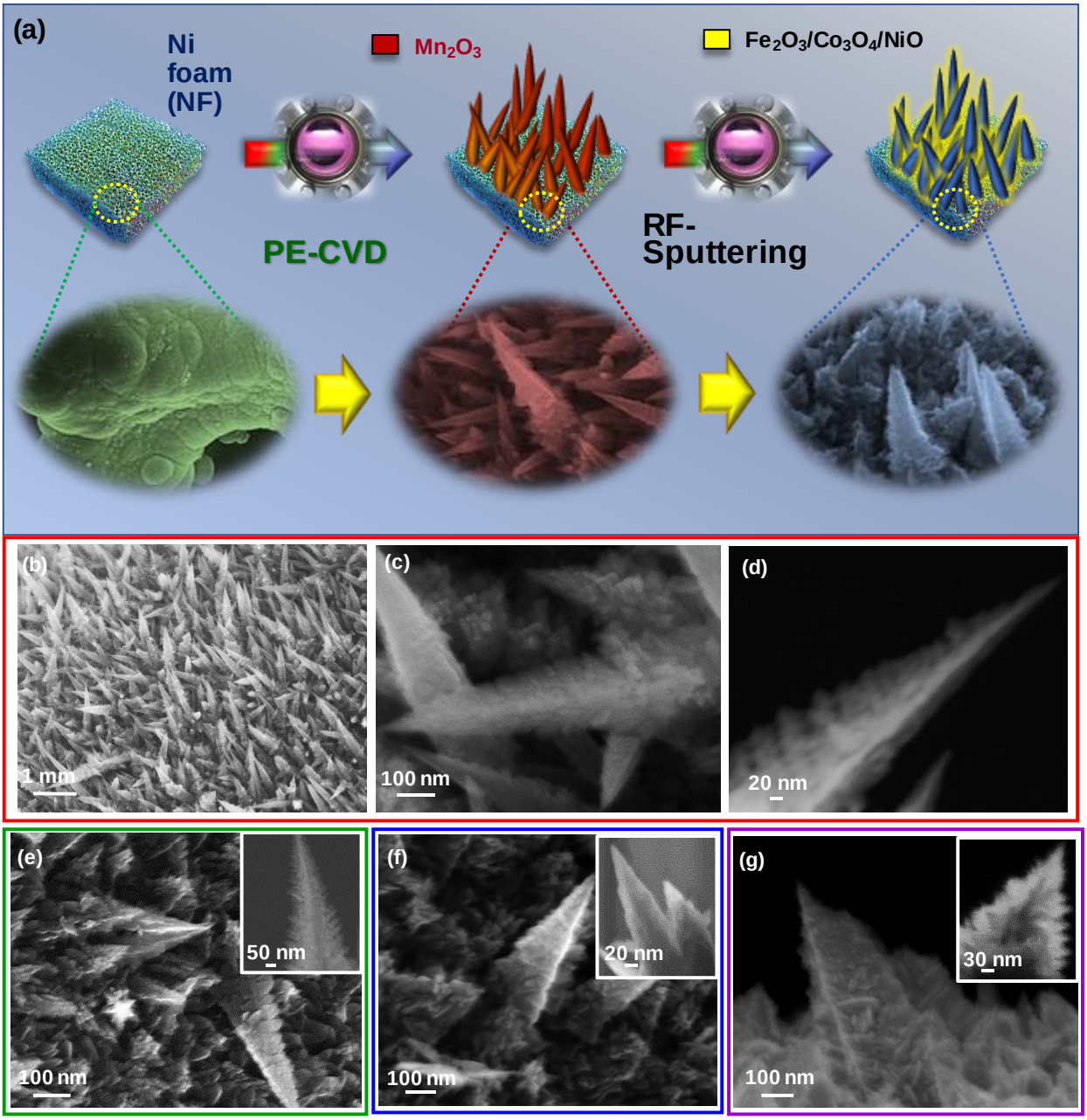

Figure 1. (a) Schematic illustration of the fabrication procedure adopted for Mn_2O_3-based electrodes functionalized with Fe_2O_3, Co_3O_4, and NiO complementary catalysts. Field emission-scanning electron microscopy (FE-SEM) images (b,c) and scanning transmission electron microscopy (STEM) micrograph (d) of bare Mn_2O_3. FE-SEM pictures of Mn_2O_3-Fe_2O_3 (e), Mn_2O_3-Co_3O_4 (f), and Mn_2O_3-NiO (g) electrodes. STEM micrographs pertaining to each nanocomposite are reported as insets in panels (e), (f) and (g).

(NPs) were introduced by radio frequency (RF)-Sputtering, and the obtained systems were

annealed under an inert atmosphere, to ensure the formation of pure Mn_2O_3. The inherent advantages of the used strategy[35-36] yielded high area quasi-1D arrays, featuring an intimate contact between Mn_2O_3 and the complementary catalysts, of crucial importance to benefit from their chemical and electronic interplay for the target applications. The best Fe_2O_3-MnO_2 systems achieve an overpotential (η) as low as ≈350 mV *vs*. the reversible hydrogen electrode (RHE) at a current density of 10 $mA \times cm^{-2}$, and a low Tafel slope of 70 $mV \times dec^{-1}$, which, to our knowledge, are among the best values reported for OER catalysts based on manganese oxides in alkaline environments.

■ EXPERIMENTAL SECTION

Sample Preparation. PE-CVD of MnO_2 nanodeposits was performed on Ni foams (Ni-4753, RECEMAT BV; lateral size = 1 cm ×1.5 cm), pre-cleaned by sonication in dichloroethane (10 min), 3.5 M HCl (10 min) and ethanol (10 min).[6,37-41] Ni foams were mounted on the grounded electrode of a custom-built two-electrode plasmochemical apparatus, and RF-power (13.56 MHz) was delivered to a second electrode. A diketonate-diamine Mn(II) compound, $Mn(hfa)_2TMEDA$ (Hhfa = 1,1,1,5,5,5-hexafluoro-2,4-pentanedione; TMEDA = *N*,*N*,*N'*,*N'*-tetramethylethylenediamine),[42-43] used as manganese precursor, was vaporized at 70°C in an external glass reservoir, and delivered into the reactor by means of an Ar flow [rate = 60 standard cubic centimeters per minute (sccm)] through metal gas lines maintained at 130°C. Additional Ar and O_2 flows (rates = 15 and 5 sccm, respectively) were separately introduced into the reaction chamber. Basing on previous results,[44] depositions were performed for 180 min at a substrate temperature of 300°C and a total pressure of 1.0 mbar, using a RF-power of 20 W. Functionalization of the obtained deposits with Fe_2O_3, Co_3O_4, and NiO was carried by RF-

Sputtering from Ar plasmas using the same instrumentation and the above obtained manganese oxide specimens as substrates. Fe (Alfa Aesar, purity = 99.995%, thickness = 0.25 mm), Co (Alfa Aesar, purity = 99.95%, thickness = 0.30 mm), or Ni (Alfa Aesar, purity = 99.994%, thickness = 0.5 mm) targets were fixed on the RF electrode. Depositions were performed using the following settings: RF-power = 20 W; total pressure = 0.3 mbar; growth temperature = 60°C; Ar flow rate = 10 sccm; process duration = 180 min for Fe sputtering, and 120 min for Co and Ni sputtering. The fabricated systems were annealed at 500°C for 60 min under Ar to ensure the formation of phase-pure Mn_2O_3.[21] For comparison, a bare manganese(III) oxide sample was obtained adopting the same deposition and thermal treatment conditions, but without any RF-Sputtering treatment.

Chemico-Physical Characterization. Field emission-scanning electron microscopy (FE-SEM) and low-resolution scanning transmission electron microscopy (STEM) analyses were carried out on a Zeiss SUPRA 40VP instrument, at primary beam voltages of 20 kV. The mean aggregate dimensions were evaluated using the ImageJ® software,[45] averaging over various independent measurements.

X-ray diffraction (XRD) patterns were recorded with a Bruker D8 Advance diffractometer equipped with a Göbel mirror, operating at 40 kV and 40 mA with CuKα radiation (λ = 1.541 Å) at an incidence angle of 1.0°, in the 2θ range of 16-42°.

During thin cross-sectional sample preparation for transmission electron microscopy (TEM), a carbon coating and a Pt protective layer (thickness = 1 µm and 2 µm, respectively) were deposited to prevent detrimental nanostructure damage. Pre-thinned lamellas were lifted-out, attached to TEM grid and then thinned down to electron transparency, performing final cleaning by focused ion beam (FIB) at 5 kV, 25 pA. The analyses, including bright field-high resolution TEM (BF-HRTEM), high angle annular dark field-STEM (HAADF-STEM) and STEM-EDXS (energy

dispersive X-ray spectroscopy) mapping experiments were carried out on an aberration double-corrected cold FEG JEM ARM200F microscope operated at 200 kV and equipped with a large angle CENTURIO EDX detector, ORIUS Gatan camera and Quantum GIF.

Surface X-ray photoelectron spectroscopy (XPS) characterization was performed by a Perkin-Elmer Φ 5600-ci spectrometer, using a standard AlKα X-ray source ($h\nu$ = 1486.6 eV). Binding Energy (BE) values (uncertainty = ±0.2 eV) were referenced to the C1s peak at 284.8 eV to correct the shift caused by charging effects.[46] After a Shirley-type background subtraction,[47] atomic percentage (at.%) values were obtained by peak area integration using Φ V5.4A sensitivity factors. Elemental molar fractions were calculated as:[35-36]

$$X_M = ((M\ at.\%) / (M\ at.\% + Mn\ at.\%)) \times 100 \quad (1)$$

where M = Fe, Co, Ni.

In-depth secondary ion mass spectrometry (SIMS) measurements were carried out by means of a IMS 4f mass spectrometer (Cameca) using a Cs^+ primary beam (14.5 keV, 25 nA, stability = 0.3%), rastering over a 175×175 μm^2 area and detecting secondary ions from a sub region close to 8×8 μm^2 to avoid detrimental crater effects. The erosion rate was estimated at various depths through the measurement of the corresponding crater height by a Tencor Alpha Step profiler, and erosion time values were converted into depth accordingly.

Electrochemical tests. Electrocatalytic activity of the target systems was tested with a standard three-electrode setup (Figure S1), using a VMP3 (BioLogic Science Instruments) electrochemical working station. Hg/HgO (MMO) and a Pt mesh were used as the reference and counter electrode, respectively. OER performances were measured using Ni foam-supported specimens as working electrodes through linear sweep voltammetry (LSV), scan rate = 1 $mV \times s^{-1}$ in freshly prepared 1 M KOH (pH = 14) solution.

The peculiar material chemico-physical characteristics and the intrinsic uncertainty in the estimation of double layer capacitance and specific capacitance[48-49] prevented from a reliable calculation of the electrochemical active surface area (ECSA). On this basis, the material catalytic activity and the measured currents were related to the geometrical surface (≈1.0×1.0 cm^2), which has indeed a practical meaning in terms of technological applications.[50]

The measured potentials (*vs*. MMO) were converted into the reversible hydrogen electrode (RHE) scale.[23] The overpotential for oxygen evolution η was computed at 10 $mA \times cm^{-2}$ using the formula:[4,51]

$$\eta\ (V) = E_{measured}\ (V\ vs.\ RHE) - 1.23 \quad (2)$$

where $E_{measured}$ is the experimental potential and 1.23 is the E° value for O_2 evolution *vs.* RHE. The data presented for the electrochemical characterization in aqueous solutions in three-electrode configuration do not include compensation for the series resistance of the solution.

Tafel slopes were obtained by plotting potential against logarithm of the current density from LSV curves.[1] Chronoamperometric analyses were carried out at a fixed potential value of 1.60 V *vs.* RHE in order to test the system time stability.

■ RESULTS AND DISCUSSION

Material characterization. In this study, the attention was initially dedicated to the investigation of the system morphology by means of FE-SEM and STEM analyses. The morphology of bare Mn_2O_3 (Figures S2 and 1b-d) was characterized by a uniform coverage of Ni foam branches with quasi-1D nanostructures (average length and diameter ≈600 and ≈150 nm respectively; mean aspect ratio = 4), assembled into high-area arrays. The obtainment of the latter paves the way to attractive OER electrocatalytic performances thanks to their high interfacial area, short diffusion

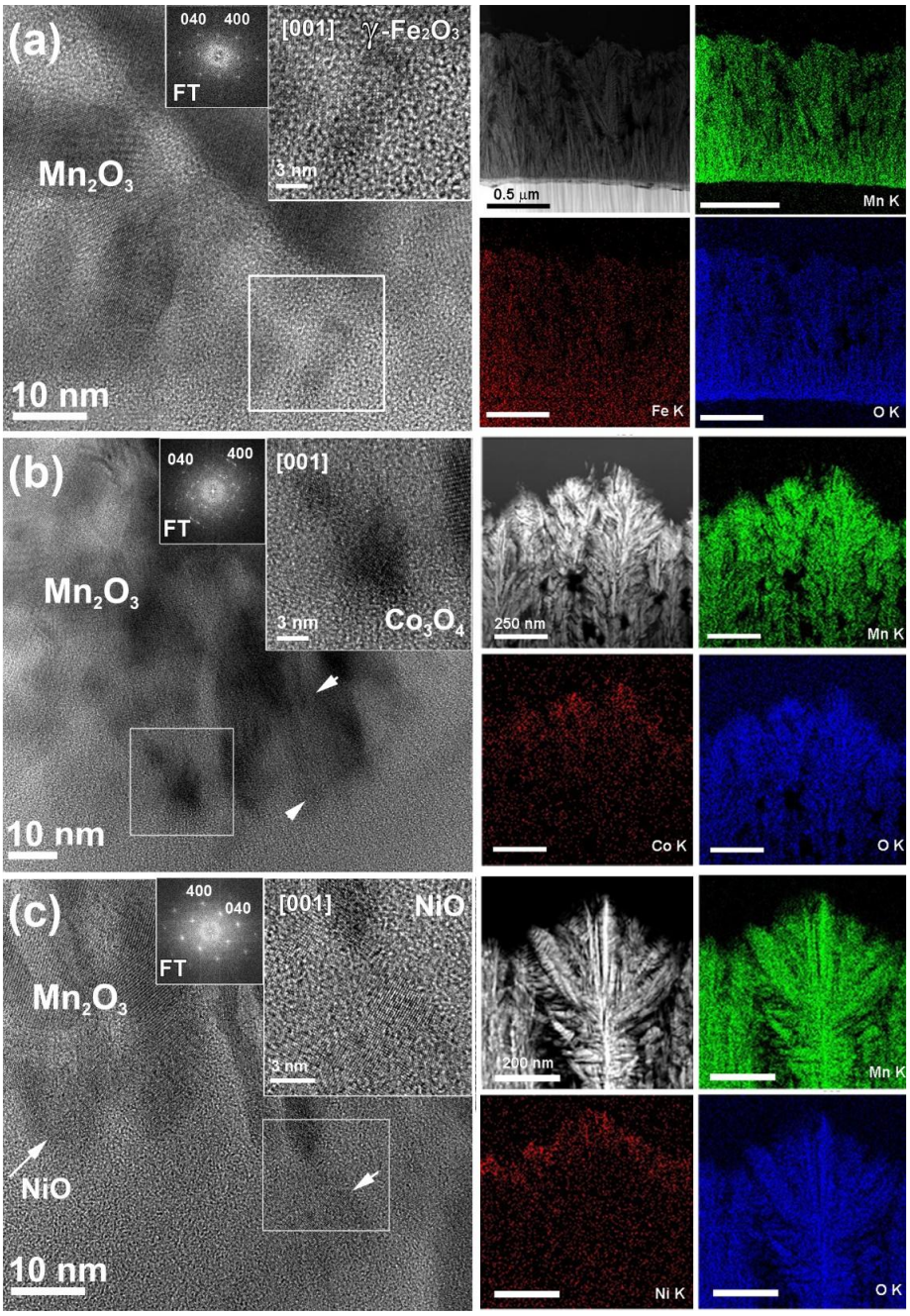

Figure 2. (left panel) Cross-sectional HRTEM images of Mn_2O_3-Fe_2O_3 (a), Mn_2O_3-Co_3O_4 (b), and Mn_2O_3-NiO (c) samples. The insets in (a), (b) and (c) are higher magnification micrographs of the areas marked by white boxes. The amorphous part in (a, b, c) corresponds to the carbon coating deposited during sample preparation. White arrows in (b) and (c) indicate Co_3O_4 and NiO NPs, respectively. FT patterns of single NPs (insets in (a, b, c)) reveal γ-Fe_2O_3 (a), Co_3O_4 (b) and NiO (c) structures oriented along the [001] zone axis. (right panel) Corresponding HAADF-STEM images together with STEM-EDXS chemical maps of MnKα, OKα and of FeKα, CoKα and NiKα for the various specimens.

paths for electrons and ions, and facilitated O_2 evolution.[4,6,16,25] In addition, Mn_2O_3 nanorods act as trapping network towards Fe, Co and Ni nanoparticles (NPs), resulting in their efficient dispersion and immobilization onto the pristine manganese oxide.[34] This peculiar quasi-1D morphology did not undergo significant alterations after RF-Sputtering (Figures 1e-g), indicating that the adopted functionalization procedure enabled to preserve the pristine Mn_2O_3 nano-organization.

Preliminary XRD analyses revealed the presence of cubic β-Mn_2O_3 as the sole crystalline phase (Figure S3).[52] The low signal intensity suggested the formation of small and defective nanocrystallites,[30] in line with XPS data (see below). After RF-Sputtering, no pattern modification and no additional peaks could be observed, suggesting a relatively low Fe, Co, Ni oxide amount along with the formation of low-sized and highly dispersed nanocrystallites.[35-36] To attain a deeper insight into the system nanostructure, TEM and EDXS analyses were performed (Figure 2). The crystal structure of Mn_2O_3 and of the complementary catalysts were determined from HRTEM images and corresponding Fast Fourier transforms (FTs) (Figure 2, left panel) patterns. For all samples, lattice parameters specific for cubic Mn_2O_3,[52] along with γ-Fe_2O_3[53] (Figure 2a), Co_3O_4[54] (Figure 2b), and NiO[55] (Figure 2c) were detected. In the first case, the occurrence of γ-Fe_2O_3 (*maghemite*) instead of the most thermodynamically stable α-Fe_2O_3 (*hematite*) was traced back to the non-equilibrium plasma conditions characterizing RF-Sputtering.[35-36] For all samples, the quasi-1D Mn_2O_3 nano-organization was confirmed by HAADF-STEM images (Figure 2, right panel), in line with FE-SEM results (see above). The uniform distribution of Mn and O throughout the sampled regions, evidenced by cross-sectional STEM-EDXS maps, was in line with the formation of phase-pure Mn_2O_3. For Fe_2O_3-Mn_2O_3, despite the weakness of the FeKα signal due to the small γ-Fe_2O_3 amount and the high NPs dispersion, the corresponding STEM-EDXS

chemical maps suggested a homogeneous distribution of γ-Fe_2O_3 nanoaggregates (5-10 nm) throughout the whole specimen. As concerns Co_3O_4-Mn_2O_3 (Figure 2b), at variance with the previous case, EDXS mapping revealed that cobalt oxide NPs (5-15 nm) were mainly concentrated in the outermost regions of the Mn_2O_3 deposit. A similar phenomenon took place even for NiO-Mn_2O_3 (Figure 2c). For this specimen, the average NiO aggregate dimensions were estimated to be 7-10 nm. As discussed below, the different spatial distribution of the complementary catalysts in the Mn_2O_3 deposits has a direct influence on the resulting electrocatalytic performances.

Material surface and in-depth chemical composition was investigated by the combined use of XPS and SIMS. XPS surface analyses evidenced in all specimens the presence of manganese and oxygen signals (Figure S4a), together with Fe, Co, and Ni ones for the functionalized systems. The Mn2p and Mn3s spectral features (Figures 3a-b; average $Mn2p_{3/2}$ BE = 641.8 eV; spin-orbit separation (SOS) = 11.6 eV; Mn3s multiplet splitting separation = 5.4 eV) were in line with the presence of pure Mn_2O_3.[15,20,28,32,56-57] The O1s signals (see Figure 3c and S4b-e; Supporting Information), revealed a main band due to lattice oxygen (I; mean BE = 529.9 eV) and an additional one (II, mean BE = 531.6 eV; on average, ≈30% of the total O content) attributed to oxygen/hydroxyl groups chemisorbed on O defects.[2,5,17,35-36,45,57-58]

The presence of the latter species is indeed beneficial in enhancing material performances in OER applications.[17] The Fe (Figure 3d; BE($Fe2p_{3/2}$) = 711.2 eV; SOS = 13.4 eV), Co (Figure 3e; BE($Co2p_{3/2}$) = 780.3 eV; SOS = 15.8 eV), and Ni (Figure 3f; BE($Ni2p_{3/2}$) = 855.0 eV; SOS = 17.4 eV; shake-up satellites at values ≈ 8 eV higher than the main spin-orbit components) peak features were in good agreement with previous literature data for Fe_2O_3,[5,36,45] Co_3O_4,[26,35,45] and NiO.[1,5,7] The mean surface molar fraction was X_M = (9±1) % (M = Fe, Co, Ni). Overall, XPS data, in line with XRD results, enabled to discard the presence of ternary Mn-M-O phases and highlighted the

formation of composite systems. In-depth compositional analyses by secondary ion mass spectrometry (SIMS) (Figure S5) revealed a good purity of the target materials (average C concentration < 100 ppm).

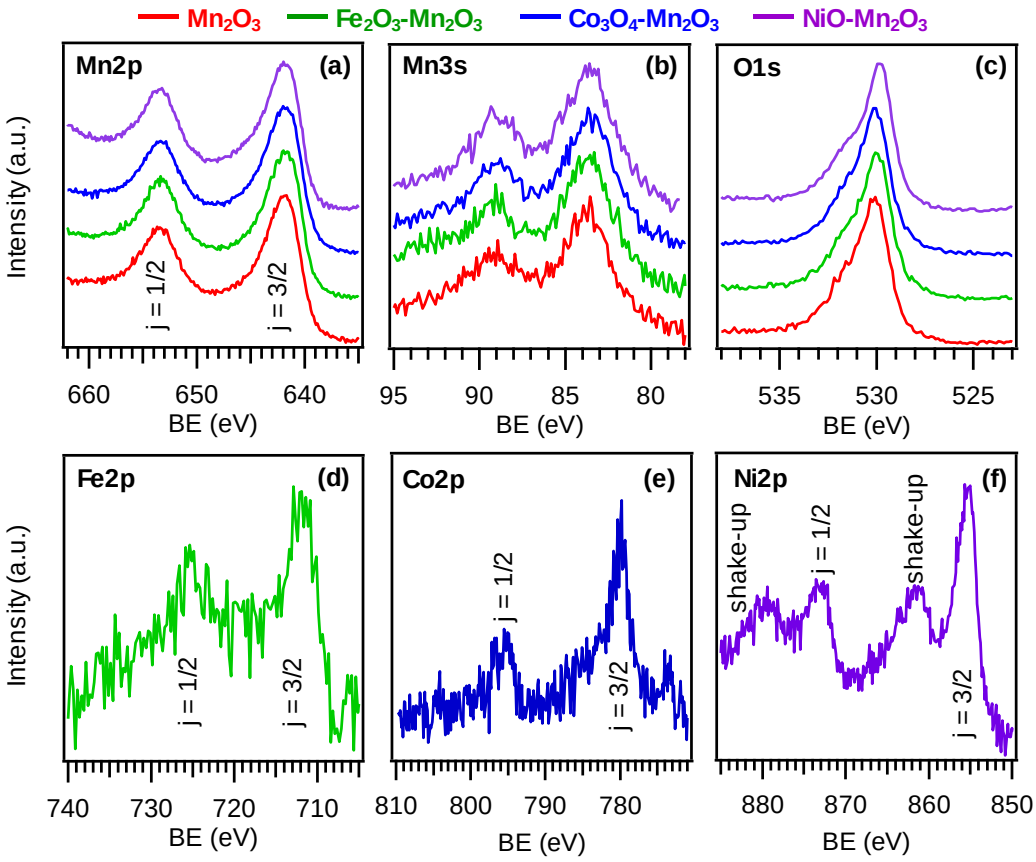

Figure 3. XPS spectra of (a) Mn2p, (b) Mn3s, (c) O1s, (d) Fe2p, (e) Co2p, (f) Ni2p for Mn_2O_3-based electrodes.

Electrochemical characterization. To evaluate OER electrocatalytic activities of the developed materials, electrochemical measurements were performed in 1 M KOH solutions. Linear sweep voltammetry (LSV) curves (Figure 4a) displayed a sharp increase of the anodic current response at an onset potential (*i.e.*, the potential needed to reach 1 mA/cm^2) of ≈1.5 V and 1.6 V *vs.* RHE for Mn_2O_3-based materials and bare Ni foam, respectively. The current densities for bare and functionalized Mn_2O_3 systems were all systematically higher than that of the Ni foam substrate

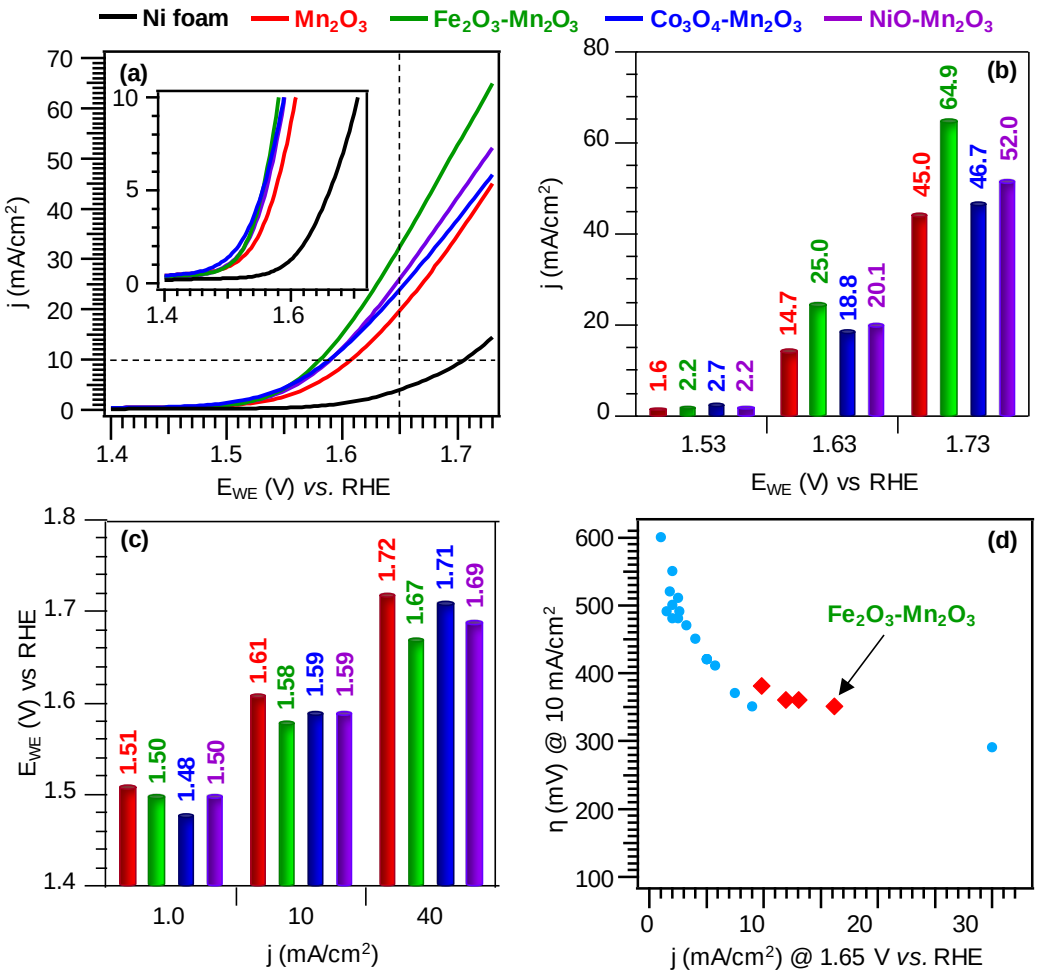

Figure 4. OER electrochemical performances of Mn_2O_3-based electrodes and bare Ni foam in 1.0 M KOH solution. (a) LSV traces (the inset shows an enlargement of the curves in the potential window 1.4-1.7 V *vs*. RHE). Bar diagrams reporting (b) current densities at different potentials, and (c) potential values at different current densities. (d) Comparison between the performances of manganese oxide-based materials reported in literature (blue markers), and the present ones (red markers; see Table S1 for details).

and increased in the order Mn_2O_3 < Co_3O_4-Mn_2O_3 < NiO-Mn_2O_3 < Fe_2O_3-Mn_2O_3, indicating a higher activity for the composite materials. This latter observation is particularly evident from the inspection of Figures 4b-c. As illustrated in Figure 4c, composite materials and, in particular Fe_2O_3-Mn_2O_3, required lower potentials than bare Mn_2O_3 to achieve fixed current density values. These data clearly show the beneficial role of metal oxide NPs on the overall OER activity, with

a current density improvement up to 45% and an overpotential drop of 30 mV with respect to pristine Mn_2O_3 for Fe_2O_3-Mn_2O_3, the best performing sample. Notably, the current densities at 1.65 V *vs.* RHE and the overpotential values (Figure 4d and Table S1) position the target materials among the most active manganese-based materials reported in the literature up to date. In addition, Mn_2O_3 functionalization promoted a decrease of Tafel slopes (Figure 5a), according to the following trend: Fe_2O_3-Mn_2O_3 (70 mV×dec^{-1}) < NiO-Mn_2O_3 (84 mV×dec^{-1}) < Co_3O_4-Mn_2O_3 ≈ Mn_2O_3 (95 mV×dec^{-1}) < Ni foam (100 mV×dec^{-1}), thus confirming the beneficial effect of the functionalizing agent on the overall catalytic activity - a lower Tafel slope value is in fact associated with faster reaction kinetics.[30,58-59] The decrease of Tafel slope values for composite samples could be ascribed to a change in the reaction mechanism[60] (the Tafel slope decreases once the rate-determining step is closer to the end step of a series of reactions)[61] and/or to a different degree of surface coverage by reaction intermediates (the higher the coverage, the lower the corresponding Tafel slope) even for the same rate-determining step.[62] If the former is the case, this could suggest an active role of functionalizing species, inducing a shift towards the last reaction of the four-step OER mechanism.[61] Remarkably, Tafel slope values were among the lowest reported so far for manganese oxide-based materials (Table S1). As shown in Figure 5b and 5c, Fe_2O_3-Mn_2O_3 exhibited the second best electrocatalytic performances among manganese oxide-based systems reported in the literature up to date and compared favorably with various benchmark IrO_2 and RuO_2 materials (similar overpotential and Tafel slope, see Table S1 and S2; Supporting Information).

The attractive performances, and activity enhancement, resulting from Mn_2O_3 functionalization with Fe, Co, and Ni oxide NPs, can be traced back to the concurrence of morphological, catalytical

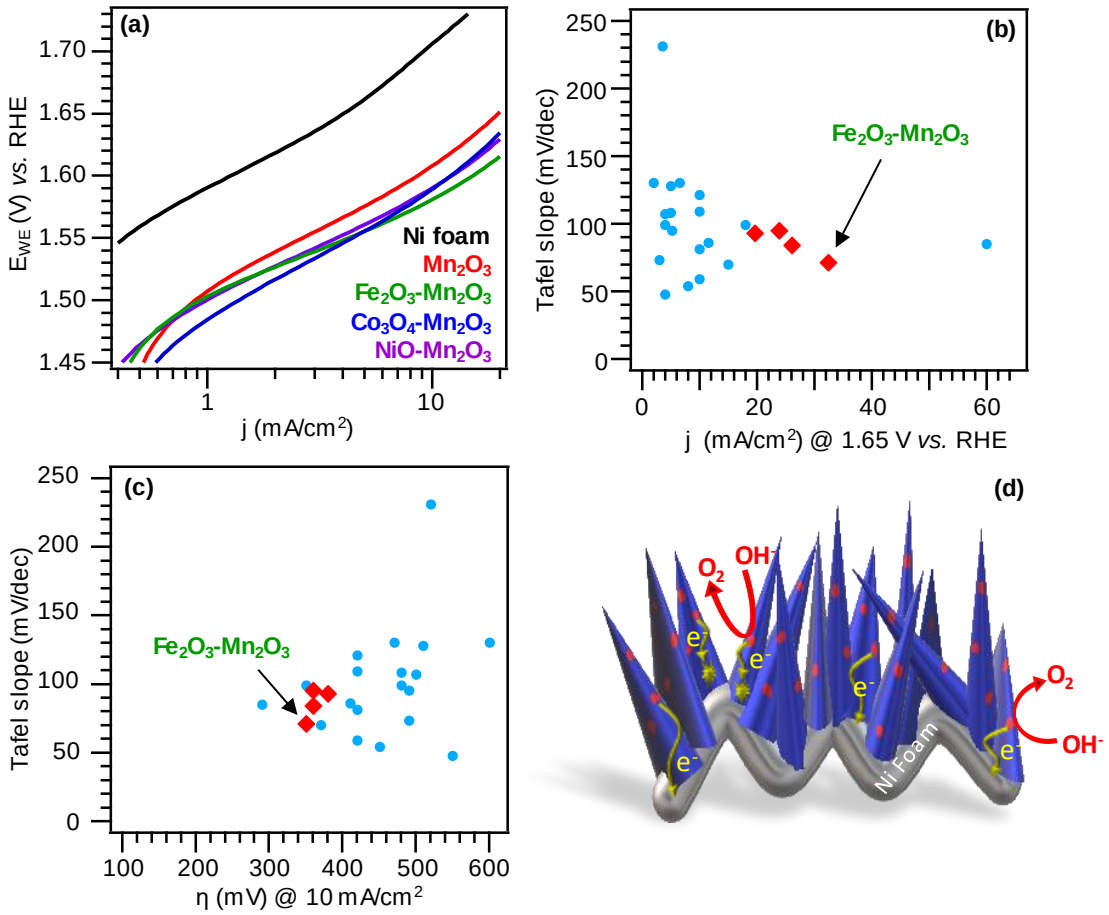

Figure 5. (a) Tafel plots for Mn_2O_3-based electrodes in 1.0 M KOH. (b,c) Comparison between the performances of manganese oxide-based catalysts reported in the literature (blue markers) with the present ones (red markers; see also Table S1). (d) Sketch of the mechanism accounting for the activity enhancement of Fe_2O_3-, Co_3O_4-, and NiO-functionalized electrodes with respect to the pristine Mn_2O_3. Blue 1D structures, red spheres, and yellow markers represent Mn_2O_3, metal oxide NPs, and recombination/trapping site, respectively.

and electronic effects. In general, the unique system morphology ensures a reduced charge carrier diffusion distance from the catalytic sites to the Ni foam substrate and, hence, to the external circuit, suppressing detrimental recombination/trapping phenomena and yielding an enhanced OER activity (Figure 5d).[63] For all the target composites, the decrease of overpotential and Tafel slope values, suggesting a change in the reaction kinetics, indicates that Fe, Co and Ni oxides likely act as OER promoters (see Figure 5d),[63-64] due to their well-known catalytic activity.[1,5,7,9-10,26,30,61]

Additional contributions are related to electronic effects resulting from the formation of oxide-oxide heterojunctions.[63] In particular, at *p*-*n* heterojunctions (Co_3O_4/Mn_2O_3 and NiO/Mn_2O_3), electrons in Mn_2O_3 (*n*-type semiconductor) will flow to Co_3O_4 or NiO (*p*-type semiconductors).[65] Similarly, at *n*-*n* heterojunction (Fe_2O_3/Mn_2O_3), electrons will flow from the higher-energy conduction band (CB) of Mn_2O_3 to the lower-energy Fe_2O_3 one.[65] The resulting enhanced separation of charge carriers yields an additional catalytic activity improvement. Last but not least, the spatial dispersion of functionalizing NPs into Mn_2O_3 is an additional factor directly influencing their mutual interactions and performances.

On the basis of the above observations, the higher catalytic activity of iron oxide-containing Mn_2O_3 nanocomposites can be ascribed to the synergistic contribution of different concurring effects. Although single-phase Co/Ni oxides usually display better OER performances than Fe ones,[59,66-69] the use of the latter as functionalizing agent has been reported to yield a higher performance improvement than the former ones,[51,69-71] as indeed observed in the present case. In addition, the more effective in-depth dispersion of Fe oxide nanoparticles into the Mn_2O_3 open structure (see above) is a key issue to facilitate electron transfer and mass transport and allow an optimal interaction of catalytic sites with the reaction environment.[64] Finally, the already mentioned electronic effects at oxide-oxide heterojunctions are expected to be higher for Fe_2O_3-Mn_2O_3 than for Co_3O_4-Mn_2O_3 and NiO-Mn_2O_3, due to the smaller dimensions of functionalizing Fe_2O_3 NPs (see TEM results) with respect to Co_3O_4 and NiO ones.[72]

Taken together, these results demonstrate the validity of our fabrication strategy to enhance the OER electrocatalytic performances of Mn(III) oxide catalysts, and highlight the potential of the developed materials for possible real-world end-uses. This conclusion is further corroborated by the operational stability of the target systems, evaluated by chronoamperometry measurements

(CA, Figure S6). After an initial period of ≈5 min, current density drops of ≈18%, 13%, 12%, and 8% were observed for Mn_2O_3, NiO-Mn_2O_3, Co_3O_4-Mn_2O_3, and Fe_2O_3-Mn_2O_3, respectively. In line with the above findings, these data highlight that Mn_2O_3 functionalization with Fe, Co, and Ni oxide complementary catalysts improves the resulting time stability, a phenomenon particularly evident for Fe_2O_3-containing systems.

To verify the occurrence of possible material deterioration upon aging, the target systems were stored at room temperature under air at atmospheric pressure for six months, and repeatedly tested as OER anodes on a monthly basis. Figure S7 contains a comparison of LSV curves recorded over a period of six months with those pertaining to as-prepared samples. For all specimens, the current density was almost constant after six months, thus excluding any significant corrosion phenomena. This conclusion, of particular importance for practical applications, was further corroborated by XPS analyses, which did not reveal any appreciable compositional variation and highlighted a good material stability (Figure S8).

■ CONCLUSIONS

In conclusion, highly active Mn_2O_3-based OER electrocatalysts were fabricated by an original plasma-assisted procedure, involving the initial PE-CVD preparation of manganese oxide on Ni foam scaffolds, the subsequent dispersion of Fe, Co, and Ni oxide NPs by RF-Sputtering, and the final thermal treatment in an inert environment. The obtained results highlight the successful fabrication of quasi-1D Mn_2O_3 nanoarrays, acting as trapping network for the anchoring of Fe_2O_3, Co_3O_4, and NiO nanoaggregates. The resulting materials were characterized by a different spatial distribution of the adopted complementary catalysts, which directly influenced OER electrocatalytic performances. The higher electroactivity enhancement with respect to bare Mn(III)

oxide, enabled by Fe_2O_3-Mn_2O_3 materials, corresponded to an overpotential as low as ≈350 mV to achieve a current density of 10 $mA \times cm^{-2}$, with a Tafel slope of ≈70 $mV \times dec^{-1}$. To our knowledge, this catalytic performance is one of the best among those reported for manganese oxide OER catalysts. This achievement was traced back to the unique system morphology and the interplay between the single oxides, maximized for Fe_2O_3-containing systems thanks to the homogeneous spatial dispersion of low-sized iron(III) oxide nanoaggregates throughout Mn_2O_3. Taken together, the present results candidate the proposed route, which is also amenable for a possible scale-up, as an effective strategy to improve the intrinsic activity of manganese(III) oxide nanostructures, opening up promising opportunities for the nano-engineering of electrocatalysts based on earth-abundant and non-precious materials. In this regard, attention will be dedicated to more detailed analyses coupled with theoretical calculations, in order to gain a detailed insight into the electronic structure and the nature of active centers in the target materials. In addition, efforts will be devoted to the investigation of the electrode stability for longer times, in view of eventual real-world applications.

■ ASSOCIATED CONTENT

Supporting Information. The Supporting Information is available free of charge on the ACS Publications website.

Experimental section, material characterization, FE-SEM micrographs, XRD patterns, additional XPS, SIMS and electrochemical data, comparison of OER performances with literature data.

■ AUTHOR INFORMATION

Corresponding Author

* E-mail: chiara.maccato@unipd.it.

ORCID

Lorenzo Bigiani: 0000-0001-7404-2340

Chiara Maccato: 0000-0001-6368-5754

Teresa Andreu: 0000-0002-2804-4545

Alberto Gasparotto: 0000-0003-4626-651X

Cinzia Sada: 0000-0002-7607-0481

Evgeny Modin: 0000-0002-7403-7610

Oleg I. Lebedev: 0000-0001-8998-5018

Joan Ramon Morante: 0000-0002-4981-4633

Davide Barreca: 0000-0002-8779-3386

Author contributions

The manuscript was written with the direct contribution of all authors. All authors have given approval to the final manuscript version.

■ ACKNOWLEDGMENTS

This work was supported by Padova University (DOR 2017–2019 and P-DiSC #03BIRD2018-UNIPD OXYGENA projects), as well as the INSTM Consortium (INSTMPD004 – NETTUNO project) and AMGA Foundation (Mn4Energy project). The authors gratefully acknowledge Dr. Daniele Valbusa and Dr. Andrea Gallo for useful technical assistance.

■ REFERENCES

(1) Tian, T.; Gao, H.; Zhou, X.; Zheng, L.; Wu, J.; Li, K.; Ding, Y. Study of the Active Sites in Porous Nickel Oxide Nanosheets by Manganese Modulation for Enhanced Oxygen Evolution Catalysis. *ACS Energy Lett.* **2018**, *3*, 2150-2158.

(2) McKendry, I. G.; Mohamad, L. J.; Thenuwara, A. C.; Marshall, T.; Borguet, E.; Strongin, D. R.; Zdilla, M. J. Synergistic In-Layer Cobalt Doping and Interlayer Iron Intercalation into Layered MnO_2 Produces an Efficient Water Oxidation Electrocatalyst. *ACS Energy Lett.* **2018**, *3*, 2280-2285.

(3) Hazarika, K. K.; Goswami, C.; Saikia, H.; Borah, B. J.; Bharali, P. Cubic Mn_2O_3 Nanoparticles on Carbon as Bifunctional Electrocatalyst for Oxygen Reduction and Oxygen Evolution Reactions. *Mol. Catal.* **2018**, *451*, 153-160.

(4) Liu, P.-P.; Li, T.-T.; Zhu, H.-L.; Zheng, Y.-Q. Manganese Oxide with Hollow Rambutan-Like Morphology as Highly Efficient Electrocatalyst for Oxygen Evolution Reaction. *J. Solid State Electrochem.* **2018**, *22*, 2999-3007.

(5) Huang, J.; Han, J.; Wang, R.; Zhang, Y.; Wang, X.; Zhang, X.; Zhang, Z.; Zhang, Y.; Song, B.; Jin, S. Improving Electrocatalysts for Oxygen Evolution Using $Ni_xFe_{3-x}O_4$/Ni Hybrid Nanostructures Formed by Solvothermal Synthesis. *ACS Energy Lett.* **2018**, *3*, 1698-1707.

(6) Liu, P.-P.; Zheng, Y.-Q.; Zhu, H.-L.; Li, T.-T. Mn_2O_3 Hollow Nanotube Arrays on Ni Foam as Efficient Supercapacitors and Electrocatalysts for Oxygen Evolution Reaction. *ACS Appl. Nano Mater.* **2019**, *2*, 744-749.

(7) Browne, M. P.; O'Rourke, C.; Wells, N.; Mills, A. Adams Method Prepared Metal Oxide Catalysts for Solar-Driven Water Splitting. *ChemPhotoChem* **2018**, *2*, 293-299.

(8) Song, X.; Yang, T.; Du, H.; Dong, W.; Liang, Z. New Binary Mn and Cr Mixed Oxide Electrocatalysts for the Oxygen Evolution Reaction. *J. Electroanal. Chem.* **2016**, *760*, 59-63.

(9) Wang, A.-L.; Xu, H.; Li, G.-R. NiCoFe Layered Triple Hydroxides with Porous Structures as High-Performance Electrocatalysts for Overall Water Splitting. *ACS Energy Lett.* **2016**, *1*, 445-453.

(10) Kou, T.; Wang, S.; Hauser, J. L.; Chen, M.; Oliver, S. R. J.; Ye, Y.; Guo, J.; Li, Y. Ni Foam-Supported Fe-Doped β-$Ni(OH)_2$ Nanosheets Show Ultralow Overpotential for Oxygen Evolution Reaction. *ACS Energy Lett.* **2019**, *4*, 622-628.

(11) Browne, M. P.; Nolan, H.; Twamley, B.; Duesberg, G. S.; Colavita, P. E.; Lyons, M. E. G. Thermally Prepared Mn_2O_3/RuO_2/Ru Thin Films as Highly Active Catalysts for the Oxygen Evolution Reaction in Alkaline Media. *ChemElectroChem* **2016**, *3*, 1847-1855.

(12) Zahran, Z. N.; Mohamed, E. A.; Naruta, Y. Electrocatalytic Water Oxidation at Low Energy Cost by a Highly Active and Robust Calcium–Manganese oxide Thin Film Sintered on an FTO Electrode with Ethyl Methyl Imidazolium Triflate Ionic Liquid. *J. Mater. Chem. A* **2017**, *5*, 15167-15174.

(13) Zahran, Z. N.; Mohamed, E. A.; Naruta, Y. Kinetics and Mechanism of Heterogeneous Water Oxidation by α-Mn_2O_3 Sintered on an FTO Electrode. *ACS Catal.* **2016**, *6*, 4470-4476.

(14) Kölbach, M.; Fiechter, S.; de Krol, R. V.; Bogdanoff, P. Evaluation of Electrodeposited α-Mn_2O_3 as a Catalyst for the Oxygen Evolution Reaction. *Catal. Today* **2017**, *290*, 2-9.

(15) Pickrahn, K. L.; Park, S. W.; Gorlin, Y.; Lee, H.-B.-R.; Jaramillo, T. F.; Bent, S. F. Active MnO_x Electrocatalysts Prepared by Atomic Layer Deposition for Oxygen Evolution and Oxygen Reduction Reactions. *Adv. Energy Mater.* **2012**, *2*, 1269-1277.

(16) Fekete, M.; Hocking, R. K.; Chang, S. L. Y.; Italiano, C.; Patti, A. F.; Arena, F.; Spiccia, L. Highly Active Screen-Printed Electrocatalysts for Water Oxidation Based on β-Manganese Oxide. *Energy Environ. Sci.* **2013**, *6*, 2222-2232.

(17) Meng, Y. T.; Song, W. Q.; Huang, H.; Ren, Z.; Chen, S. Y.; Suib, S. L. Structure-Property Relationship of Bifunctional MnO_2 Nanostructures: Highly Efficient, Ultra-Stable Electrochemical Water Oxidation and Oxygen Reduction Reaction Catalysts Identified in Alkaline Media. *J. Am. Chem. Soc.* **2014**, *136*, 11452-11464.

(18) He, J.; Wang, M.; Wang, W.; Miao, R.; Zhong, W.; Chen, S.-Y.; Poges, S.; Jafari, T.; Song, W.; Liu, J.; Suib, S. L. Hierarchical Mesoporous NiO/MnO_2@PANI Core–Shell Microspheres, Highly Efficient and Stable Bifunctional Electrocatalysts for Oxygen Evolution and Reduction Reactions. *ACS Appl. Mater. Interfaces* **2017**, *9*, 42676-42687.

(19) Li, P.; Jin, Z.; Qian, Y.; Fang, Z.; Xiao, D.; Yu, G. Probing Enhanced Site Activity of Co–Fe Bimetallic Subnanoclusters Derived from Dual Cross-Linked Hydrogels for Oxygen Electrocatalysis. *ACS Energy Lett.* **2019**, *4*, 1793-1802.

(20) Wang, W.; Kuai, L.; Cao, W.; Huttula, M.; Ollikkala, S.; Ahopelto, T.; Honkanen, A.-P.; Huotari, S.; Yu, M.; Geng, B. Mass-Production of Mesoporous $MnCo_2O_4$ Spinels with Manganese(IV)- and Cobalt(II)-Rich Surfaces for Superior Bifunctional Oxygen Electrocatalysis. *Angew. Chem. Int. Ed.* **2017**, *56*, 14977-14981.

(21) Mattelaer, F.; Bosserez, T.; Ronge, J.; Martens, J. A.; Dendooven, J.; Detavernier, C. Manganese Oxide Films with Controlled Oxidation State for Water Splitting Devices Through a Combination of Atomic Layer Deposition and Post-Deposition Annealing. *RSC Adv.* **2016**, *6*, 98337-98343.

(22) Li, C.; Han, X.; Cheng, F.; Hu, Y.; Chen, C.; Chen, J. Phase and Composition Controllable Synthesis of Cobalt Manganese Spinel Nanoparticles towards Efficient Oxygen Electrocatalysis. *Nat. Commun.* **2015**, *6*, 7345.

(23) Lian, S.; Browne, M. P.; Domínguez, C.; Stamatin, S. N.; Nolan, H.; Duesberg, G. S.; Lyons, M. E. G.; Fonda, E.; Colavita, P. E. Template-free Synthesis of Mesoporous Manganese Oxides with Catalytic Activity in the Oxygen Evolution Reaction. *Sustainable Energy Fuels* **2017**, *1*, 780-788.

(24) Ramírez, A.; Hillebrand, P.; Stellmach, D.; May, M. M.; Bogdanoff, P.; Fiechter, S. Evaluation of MnO_x, Mn_2O_3, and Mn_3O_4 Electrodeposited Films for the Oxygen Evolution Reaction of Water. *J. Phys. Chem. C* **2014**, *118*, 14073-14081.

(25) Chen, S.; Zhai, T.; Lu, X.-H.; Zhang, M.-Z.; Li, Z.-Y.; Xu, C.-W.; Tong, Y. Large-Area Manganese Oxide Nanorod Arrays as Efficient Electrocatalyst for Oxygen Evolution Reaction. *Int. J. Hydrogen Energy* **2012**, *37*, 13350-13354.

(26) Tahir, M.; Pan, L.; Zhang, R.; Wang, Y.-C.; Shen, G.; Aslam, I.; Qadeer, M. A.; Mahmood, N.; Xu, W.; Wang, L.; Zhang, X.; Zou, J.-J. High-Valence-State NiO/Co_3O_4 Nanoparticles on Nitrogen-Doped Carbon for Oxygen Evolution at Low Overpotential. *ACS Energy Lett.* **2017**, *2*, 2177-2182.

(27) Adpakpang, K.; Oh, S. M.; Agyeman, D. A.; Jin, X.; Jarulertwathana, N.; Kim, I. Y.; Sarakonsri, T.; Kang, Y.-M.; Hwang, S.-J. Holey 2D Nanosheets of Low-Valent Manganese Oxides with an Excellent Oxygen Catalytic Activity and a High Functionality as a Catalyst for Li–O_2 Batteries. *Adv. Funct. Mater.* **2018**, *28*, 1707106.

(28) Sim, H.; Lee, J.; Yu, T.; Lim, B. Manganese Oxide with Different Composition and Morphology as Electrocatalyst for Oxygen Evolution Reaction. *Korean J. Chem. Eng.* **2018**, *35*, 257-262.

(29) Ghosh, S.; Kar, P.; Bhandary, N.; Basu, S.; Sardar, S.; Maiyalagan, T.; Majumdar, D.; Bhattacharya, S. K.; Bhaumik, A.; Lemmens, P.; Pal, S. K. Microwave-Assisted Synthesis of Porous Mn_2O_3 Nanoballs as Bifunctional Electrocatalyst for Oxygen Reduction and Evolution Reaction. *Catal. Sci. Technol.* **2016**, *6*, 1417-1429.

(30) Luo, Z. S.; Irtem, E.; Ibanez, M.; Nafria, R.; Marti-Sanchez, S.; Genc, A.; de la Mata, M.; Liu, Y.; Cadavid, D.; Llorca, J.; Arbiol, J.; Andreu, T.; Morante, J. R.; Cabot, A. Mn_3O_4@$CoMn_2O_4$-Co_xO_y Nanoparticles: Partial Cation Exchange Synthesis and Electrocatalytic Properties toward the Oxygen Reduction and Evolution Reactions. *ACS Appl. Mater. Interfaces* **2016**, *8*, 17435-17444.

(31) Kuo, C. H.; Mosa, I. M.; Poyraz, A. S.; Biswas, S.; E-Sawy, A. M.; Song, W. Q.; Luo, Z.; Chen, S. Y.; Rusling, J. F.; He, J.; Suib, S. L. Robust Mesoporous Manganese Oxide Catalysts for Water Oxidation. *ACS Catal.* **2015**, *5*, 1693-1699.

(32) Jahan, M.; Tominaka, S.; Henzie, J. Phase Pure α-Mn_2O_3 Prisms and their Bifunctional Electrocatalytic Activity in Oxygen Evolution and Reduction Reactions. *Dalton Trans.* **2016**, *45*, 18494-18501.

(33) Liu, G. Y.; Hall, J.; Nasiri, N.; Gengenbach, T.; Spiccia, L.; Cheah, M. H.; Tricoli, A. Scalable Synthesis of Efficient Water Oxidation Catalysts: Insights into the Activity of Flame-Made Manganese Oxide Nanocrystals. *ChemSusChem* **2015**, *8*, 4162-4171.

(34) Tovini, M. F.; Patil, B.; Koz, C.; Uyar, T.; Yılmaz, E. Nanohybrid Structured RuO_2/Mn_2O_3/CNF as a Catalyst for Na–O_2 Batteries. *Nanotechnology* **2018**, *29*, 475401.

(35) Carraro, G.; Maccato, C.; Gasparotto, A.; Kaunisto, K.; Sada, C.; Barreca, D. Plasma-Assisted Fabrication of Fe_2O_3-Co_3O_4 Nanomaterials as Anodes for Photoelectrochemical Water Splitting. *Plasma Processes Polym.* **2016**, *13*, 191-200.

(36) Carraro, G.; Gasparotto, A.; Maccato, C.; Bontempi, E.; Bilo, F.; Peeters, D.; Sada, C.; Barreca, D. A Plasma-Assisted Approach for the Controlled Dispersion of CuO Aggregates into β Iron(III) Oxide Matrices. *CrystEngComm* **2014**, *16*, 8710-8716.

(37) Zhang, D.; Zhang, J.; Wang, H.; Cui, C.; Jiao, W.; Gao, J.; Liu, Y. Novel Ni Foam Based Nickel Oxalate Derived Porous NiO Nanostructures as Highly Efficient Electrodes for the Electrooxidation of Methanol/Ethanol and Urea. *J. Alloys Compd.* **2019**, *806*, 1419-1429.

(38) Chaudhari, N. K.; Jin, H.; Kim, B.; Lee, K. Nanostructured Materials on 3D Nickel Foam as Electrocatalysts for Water Splitting. *Nanoscale* **2017**, *9*, 12231-12247.

(39) Urbain, F.; Du, R.; Tang, P.; Smirnov, V.; Andreu, T.; Finger, F.; Jimenez Divins, N.; Llorca, J.; Arbiol, J.; Cabot, A.; Morante, J. R. Upscaling High Activity Oxygen Evolution Catalysts Based on $CoFe_2O_4$ Nanoparticles Supported on Nickel Foam for Power-to-Gas Electrochemical Conversion with Energy Efficiencies above 80%. *Appl. Catal., B* **2019**, *259*, 118055.

(40) Li, Z.; Shao, M.; An, H.; Wang, Z.; Xu, S.; Wei, M.; Evans, D. G.; Duan, X. Fast Electrosynthesis of Fe-containing Layered Double Hydroxide Arrays toward Highly Efficient Electrocatalytic Oxidation Reactions. *Chem. Sci.* **2015**, *6*, 6624-6631.

(41) Yu, M. Q.; Li, Y. H.; Yang, S.; Liu, P. F.; Pan, L. F.; Zhang, L.; Yang, H. G. Mn_3O_4 Nano-Octahedrons on Ni Foam as an Efficient Three-Dimensional Oxygen Evolution Electrocatalyst. *J. Mater. Chem. A* **2015**, *3*, 14101-14104.

(42) Barreca, D.; Carraro, G.; Fois, E.; Gasparotto, A.; Gri, F.; Seraglia, R.; Wilken, M.; Venzo, A.; Devi, A.; Tabacchi, G.; Maccato, C. Manganese(II) Molecular Sources for Plasma-Assisted CVD of Mn Oxides and Fluorides: From Precursors to Growth Process. *J. Phys. Chem. C* **2018**, *122*, 1367-1375.

(43) Maccato, C.; Bigiani, L.; Carraro, G.; Gasparotto, A.; Seraglia, R.; Kim, J.; Devi, A.; Tabacchi, G.; Fois, E.; Pace, G.; Di Noto, V.; Barreca, D. Molecular Engineering of Mn^{II} Diamine Diketonate Precursors for the Vapor Deposition of Manganese Oxide Nanostructures. *Chem. Eur. J.* **2017**, *23*, 17954-17963.

(44) Barreca, D.; Gri, F.; Gasparotto, A.; Carraro, G.; Bigiani, L.; Altantzis, T.; Žener, B.; Lavrenčič Štangar, U.; Alessi, B.; Padmanaban, D. B.; Mariotti, D.; Maccato, C. Multi-Functional MnO_2 Nanomaterials for Photo-Activated Applications by a Plasma-Assisted Fabrication Route. *Nanoscale* **2019**, *11*, 98-108.

(45) http://srdata.nist.gov/xps.

(46) Briggs, D.; Seah, M. P. *Practical Surface Analysis: Auger and X-ray Photoelectron Spectroscopy*, John Wiley & Sons: New York, 2nd ed. 1990.

(47) Shirley, D. A. High-Resolution X-ray Photoemission Spectrum of the Valence Bands of Gold. *Phys. Rev. B* **1972**, *5*, 4709-4714.

(48) McCrory, C. C. L.; Jung, S.; Peters, J. C.; Jaramillo, T. F. Benchmarking Heterogeneous Electrocatalysts for the Oxygen Evolution Reaction. *Journal of the American Chemical Society* **2013**, *135*, 16977-16987.

(49) Connor, P.; Schuch, J.; Kaiser, B.; Jaegermann, W. The Determination of Electrochemical Active Surface Area and Specific Capacity Revisited for the System MnO_x as an Oxygen Evolution Catalyst. *Z. Phys. Chem.* **2020**, *234*, 979.

(50) Simon, Q.; Barreca, D.; Bekermann, D.; Gasparotto, A.; Maccato, C.; Comini, E.; Gombac, V.; Fornasiero, P.; Lebedev, O. I.; Turner, S.; Devi, A.; Fischer, R. A.; Van Tendeloo, G. Plasma-Assisted Synthesis of Ag/ZnO Nanocomposites: First Example of Photo-Induced H_2 Production and Sensing. *Int. J. Hydrogen Energy* **2011**, *36*, 15527-15537.

(51) Bandal, H. A.; Jadhav, A. R.; Tamboli, A. H.; Kim, H. Bimetallic iron cobalt oxide self-supported on Ni-Foam: An efficient bifunctional electrocatalyst for oxygen and hydrogen evolution reaction. *Electrochimica Acta* **2017**, *249*, 253-262.

(52) JCPDS card N° 041-1442.

(53) ICSD card N° 250541.

(54) ICSD card N° 36256.

(55) ICSD card N° 87108.

(56) Hosseini-Benhangi, P.; Kung, C. H.; Alfantazi, A.; Gyenge, E. L. Controlling the Interfacial Environment in the Electrosynthesis of MnO_x Nanostructures for High-Performance Oxygen Reduction/Evolution Electrocatalysis. *ACS Appl. Mater. Interfaces* **2017**, *9*, 26771-26785.

(57) Cheng, C.; Huang, Y.; Wang, N.; Jiang, T.; Hu, S.; Zheng, B.; Yuan, H.; Xiao, D. Facile Fabrication of Mn_2O_3 Nanoparticle-Assembled Hierarchical Hollow Spheres and Their Sensing for Hydrogen Peroxide. *ACS Appl. Mater. Interfaces* **2015**, *7*, 9526-9533.

(58) Zhang, T.; Li, Z.; Wang, L.; Sun, P.; Zhang, Z.; Wang, S. Spinel $MnCo_2O_4$ Nanoparticles Supported on Three-Dimensional Graphene with Enhanced Mass Transfer as an Efficient Electrocatalyst for the Oxygen Reduction Reaction. *ChemSusChem* **2018**, *11*, 2730-2736.

(59) Song, F.; Bai, L.; Moysiadou, A.; Lee, S.; Hu, C.; Liardet, L.; Hu, X. Transition Metal Oxides as Electrocatalysts for the Oxygen Evolution Reaction in Alkaline Solutions: An Application-Inspired Renaissance. *J. Am. Chem. Soc.* **2018**, *140*, 7748-7759.

(60) Balaghi, S. E.; Triana, C. A.; Patzke, G. R. Molybdenum-Doped Manganese Oxide as a Highly Efficient and Economical Water Oxidation Catalyst. *ACS Catal.* **2020**, *10*, 2074-2087.

(61) Suen, N.-T.; Hung, S.-F.; Quan, Q.; Zhang, N.; Xu, Y.-J.; Chen, H. M. Electrocatalysis for the Oxygen Evolution Reaction: Recent Development and Future Perspectives. *Chem. Soc. Rev.* **2017**, *46*, 337-365.

(62) Shinagawa, T.; Garcia-Esparza, A. T.; Takanabe, K. Insight on Tafel Slopes from a Microkinetic Analysis of Aqueous Electrocatalysis for Energy Conversion. *Sci. Rep.* **2015**, *5*, 13801.

(63) Xu, Y.; Li, A.; Yao, T.; Ma, C.; Zhang, X.; Shah, J. H.; Han, H. Strategies for Efficient Charge Separation and Transfer in Artificial Photosynthesis of Solar Fuels. *ChemSusChem* **2017**, *10*, 4277-4305.

(64) Tang, C.; Wang, H.-S.; Wang, H.-F.; Zhang, Q.; Tian, G.-L.; Nie, J.-Q.; Wei, F. Spatially Confined Hybridization of Nanometer-Sized NiFe Hydroxides into Nitrogen-Doped Graphene Frameworks Leading to Superior Oxygen Evolution Reactivity. *Adv. Mater.* **2015**, *27*, 4516-4522.

(65) Li, Z.; Li, H.; Wu, Z.; Wang, M.; Luo, J.; Torun, H.; Hu, P.; Yang, C.; Grundmann, M.; Liu, X.; Fu, Y. Advances in Designs and Mechanisms of Semiconducting Metal Oxide Nanostructures for High-Precision Gas Sensors Operated at Room Temperature. *Mater. Horiz.* **2019**, *6*, 470-506.

(66) Cheng, Y.; Jiang, S. P. Advances in electrocatalysts for oxygen evolution reaction of water electrolysis-from metal oxides to carbon nanotubes. *Prog. Nat. Sci.* **2015**, *25*, 545-553.

(67) Subbaraman, R.; Tripkovic, D.; Chang, K.-C.; Strmcnik, D.; Paulikas, A. P.; Hirunsit, P.; Chan, M.; Greeley, J.; Stamenkovic, V.; Markovic, N. M. Trends in activity for the water

electrolyser reactions on 3d M(Ni,Co,Fe,Mn) hydr(oxy)oxide catalysts. *Nat. Mater.* **2012**, *11*, 550-557.

(68) Lyons, M. E. G.; Brandon, M. P. A comparative study of the oxygen evolution reaction on oxidised nickel, cobalt and iron electrodes in base. *J. Electroanal. Chem.* **2010**, *641*, 119-130.

(69) Galán-Mascarós, J. R. Water Oxidation at Electrodes Modified with Earth-Abundant Transition-Metal Catalysts. *ChemElectroChem* **2015**, *2*, 37-50.

(70) Diaz-Morales, O.; Ledezma-Yanez, I.; Koper, M. T. M.; Calle-Vallejo, F. Guidelines for the Rational Design of Ni-Based Double Hydroxide Electrocatalysts for the Oxygen Evolution Reaction. *ACS Catal.* **2015**, *5*, 5380-5387.

(71) Banerjee, S.; Debata, S.; Madhuri, R.; Sharma, P. K. Electrocatalytic behavior of transition metal (Ni, Fe, Cr) doped metal oxide nanocomposites for oxygen evolution reaction. *Appl. Surf. Sci.* **2018**, *449*, 660-668.

(72) Zhang, Z.; Yates, J. T. Band Bending in Semiconductors: Chemical and Physical Consequences at Surfaces and Interfaces. *Chem. Rev.* **2012**, *112*, 5520-5551.

TOC GRAPHIC